Case Study of Moisture and Heat Budgets within Atmospheric Rivers

QIANWEN LUO AND WEN-WEN TUNG

Department of Earth, Atmospheric, and Planetary Sciences, Purdue University, West Lafayette, Indiana

(Manuscript received 14 December 2014, in final form 29 April 2015)

ABSTRACT

This work studies moisture and heat budgets within two atmospheric rivers (ARs) that made landfall on the west coast of North America during January 2009. Three-dimensional kinematic and thermodynamic fields were constructed using ECMWF Year of Tropical Convection data and global gridded precipitation datasets. Differences between the two ARs are observed, even though both had embedded precipitating convective organizations of the same spatial scale. AR1 extended from 20° to 50°N in an almost west–east orientation. It had excessive warm and moist near-surface conditions. Its precipitating systems were mainly distributed on the southwest and northeast sides of the AR, and tended to exhibit stratiform-type vertical heat and moisture transports. In contrast, AR2 spanned latitudes between 20° and 60°N in a north–south orientation. It was narrower and shorter than AR1, and was mostly covered by pronounced precipitating systems, dominated by a deep convection type of heating throughout the troposphere. In association with these distinctions, the atmosphere over the northeastern Pacific on average experienced episodic cooling and drying despite the occurrence of AR1, yet underwent heating and drying during AR2, when latent heating was strong. Downward sensible heat flux and weak upward surface latent heat flux were observed particularly in AR1. In addition, cloud radiative forcing (CRF) was very weak in AR1, whereas it was strongly negative in AR2. In short, it is found that the oceanic convection in ARs both impacts the moisture transport of ARs, as well as modifies the heat balance in the midlatitudes through latent heat release, convective heat transport, surface heat fluxes, and CRF.

1. Introduction

Atmospheric rivers (ARs) are narrow channels of enhanced moisture flux in the atmosphere (Newell et al. 1992; Zhu and Newell 1994). They perform ocean-to-ocean and ocean-to-land moisture transports (Newman et al. 2012), accounting for >90% of the total meridional moisture flux in the midlatitudes (Zhu and Newell 1998). They are typically parts of the warm conveyor belts (WCBs), which are strongly ascending airstreams near winter extratropical cyclones. The WCBs transport and redistribute heat globally, and are featured by intense latent heat release and precipitation formation (e.g., Carlson 1980; Browning 1990; Eckhardt et al. 2004; Pfahl et al. 2014). Over the past few decades, increasing attention has been paid particularly to the landfalling ARs, as these kinds of ARs often lead to strong multiday continental precipitation, extreme flooding, and impacts on regional water resources (e.g., Ralph et al. 2006; Dettinger et al. 2011; Neiman et al. 2011; Lavers and Villarini 2013).

Many recent observational (e.g., Neiman et al. 2008; Ralph et al. 2011; Newman et al. 2012) and model trajectory studies (e.g., Bao et al. 2006; Knippertz and Wernli 2010; Ryoo et al. 2011; Sodemann and Stohl 2013) have been performed to investigate the moisture sources as well as the transport mechanisms of ARs. For example, using research aircraft observations, Ralph et al. (2011) found that tropical (defined as 23.5°N–23.5°S) moisture can be transported to the subtropics in an AR event. Combining satellite observations and trajectory analysis, Bao et al. (2006) pointed out that the local moisture convergence plays a primary role in forming the enhanced integrated water vapor (IWV) band. By taking the water vapor tagging approach, Sodemann and Stohl (2013) studied the interrelation between midlatitude cyclones and ARs during boreal winter. Their results suggested that an AR can be maintained by advection of moisture along multiple extratropical cyclones and

Corresponding author address: Qianwen Luo, Department of Earth, Atmospheric, and Planetary Sciences, Purdue University, 550 Stadium Mall Dr., West Lafayette, IN 47907.
E-mail: luo43@purdue.edu

DOI: 10.1175/MWR-D-15-0006.1

depleted by the oceanic precipitation in association with several WCBs. Cordeira et al. (2013) looked at the development, evolution, and merger of two ARs in proximity to tropical cyclones. Based on the trajectory analysis and moisture budget computed from reanalysis and satellite observations along the ARs, they found that the tropical cyclones can influence the midlatitude ARs through its interactions with the North Pacific jet stream. Before the two ARs merged, evaporation and the IWV flux convergence associated with frontogenesis were the moisture sources of the ARs, with the latter being the primary one. In contrast, precipitation collocated with troposphere-deep upright ascent removed moisture effectively from the ARs (see their Table 2).

Although the aforementioned studies have largely improved our understanding of the roles of synoptic-scale circulation in AR formation and maintenance, the multiscale interactions between oceanic precipitating convective systems and the atmospheric motions in ARs remain unclear. The oceanic precipitation coverage in an AR can be substantially large (e.g., ~81% in the second AR or AR2 in our study). The multiscale interactions between clouds, convective organizations, and the ambient atmosphere are evidently important for weather forecasting and climate projection. Here we ask how the spatial characteristics, the amounts, and the dominant types of the precipitating clouds and convection in the ARs 1) influence the heat and moisture transport within ARs and 2) modify the ambient atmospheric heat and moisture budgets. For the latter, we also investigate the cloud radiative forcing (CRF).

We conduct a detailed case diagnosis on the precipitating systems of two ARs in January 2009, during the Year of Tropical Convection (YOTC; Waliser and Moncrieff 2008; Moncrieff 2010) over the northeastern (NE) Pacific region (20°–60°N, 180°–120°W). The apparent heat source Q_1 and apparent moisture sink Q_2 are computed and analyzed for evidence of the dominant cloud types and to elucidate the collective impacts of subgrid-scale eddies on the surrounding environment. Then comparisons among the column-integrated Q_1 and Q_2, the radiation budget, and surface heat fluxes are made. This paper is organized as follows. In section 2, we describe the data and methods employed for AR-structure construction as well as for heat and moisture budget residuals computations. In section 3, we give a background overview for January 2009 and the synoptic-scale merging process of enhanced IWV bands. In section 4, we present the average vertical profiles of Q_1 and Q_2 around the local maxima of IWV or the AR ridge, and examine the vertically integrated heat and moisture budgets. Discussions and conclusions are in sections 5 and 6, respectively.

2. Data and methods

a. Data

1) ECMWF YOTC DATA

This study used the European Centre for Medium-Range Weather Forecasts (ECMWF) high-resolution YOTC (e.g., Waliser and Moncrieff 2008; Moncrieff 2010) dataset as the main data source. The YOTC dataset is available for a two-year period, from 1 May 2008 to 30 April 2010. It is produced by the ECMWF Integrated Forecast System, which comprises a 4D-Var data assimilation system, with high horizontal resolution of TL799 (~25 km, May 2008–December 2009) and TL1279 (~16 km, January 2010–April 2010) and L91 model levels (91 vertical levels with the model top at 0.01 hPa).

The YOTC database includes 6-hourly global analysis (hereafter YOTC analysis) and up to 10-day forecasts (hereafter YOTC forecast, starting at 1200 UTC every day since 1 May 2008). The multiday forecasts are output at 3-h intervals. (In this study, we retrieved the analysis and forecast data at 1° × 1° horizontal grids with 25 pressure levels and surface level from http://apps.ecmwf.int/datasets/data/yotc-od/.)

2) NOAA CMORPH PRECIPITATION

NOAA Climate Prediction Center morphing technique (CMORPH; Joyce et al. 2004) is one of the most commonly used and frequently validated dataset for global precipitation (e.g., Ebert et al. 2007; Tian et al. 2007; Sapiano and Arkin 2009). This product is derived from four types of passive microwave measurements: Tropical Rainfall Measuring Mission Microwave Imager, Advanced Microwave Sounding Unit, the Special Sensor Microwave Imager, and the Advanced Microwave Scanning Radiometer. It uses the "morphing" techniques to solve the coverage gap problem and to provide microwave-derived precipitation fields with 0.25° × 0.25° spatial resolution from 60°N to 60°S and 3-hourly temporal resolution from 1 December 2002 to the present. Because of its spatial and temporal resolutions, midlatitude data coverage, as well as smooth spatial patterns, CMORPH is suitable for short-term precipitation detection (Tian et al. 2007). To compare CMORPH data with YOTC data, we downsample CMORPH to match the resolutions of YOTC.

3) GPCP DAILY PRECIPITATION

The Global Precipitation Climatology Project (GPCP) One-Degree Daily Precipitation version 1.2 dataset (Huffman et al. 2001) with 1° × 1° spatial resolution is available daily from October 1996 to the delayed present.

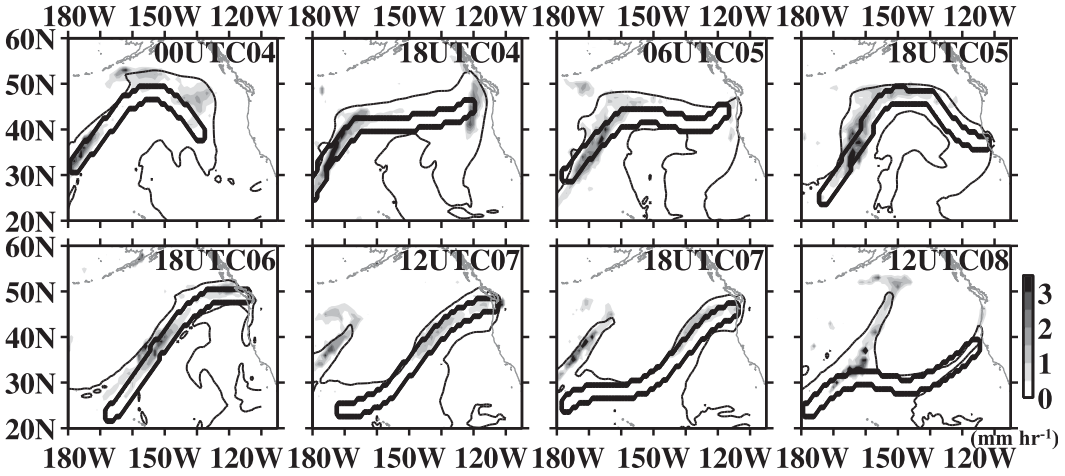

FIG. 1. Time evolution of AR1 from 0000 UTC 4 Jan to 1200 UTC 8 Jan 2009: CMORPH precipitation(mm h^{-1}) is shaded. The AR1 ridge is the thick contour and IWV = 20 mm is the thin contour.

Using the threshold-matched precipitation index algorithm, precipitation between 40°N and 40°S are estimated from geosynchronous-orbit IR and low-orbit IR. The rescaled daily Television and Infrared Observation Satellite Operational Vertical Sounder and Atmospheric Infrared Sounder are used as the primary data sources for 40°–90° in each hemisphere. Between 40°and 50° in each hemisphere, smoothing is performed to solve the data inconsistency problem. We use the GPCP data mainly because of its high-latitude data coverage from 60° to 90°N.

b. Methods

1) AR DEFINITIONS AND THE AR-RIDGE CONSTRUCTION

There exist several criteria to identify ARs. Zhu and Newell (1998) defined an AR as a filament-like structure of strong moisture flux. Ralph et al. (2004) defined an AR as an elongated and narrow region (length $\geq$ 2000 km $\times$ width $<$ 1000 km) with IWV $\geq$ 20 mm. We use the latter definition as the first step to identify AR events and then augment the identified ARs in space and time by loosening the geometrical constraint. At each instance, the broader definition captures a continuum of IWV $\geq$ 20 mm over the NE Pacific region with an AR embedded, which we call the enhanced IWV surrounding ARs (hereafter AR-IWV). This enables us to consider inclusively the moisture reservoir of an AR and the time steps when an AR curved or deformed. Within each AR-IWV, we further define a narrow segment of maximum IWV by interpolating 2° $\times$ 2° tiles, each of which is centered on a local IWV maximum. This concentrated area is denoted as the AR ridge, which is marked with the thick contours in Figs. 1 and 2. The maximum precipitation (shaded area) tends to fall inside an AR ridge, which enables us to examine the propagation and evolution of precipitating systems embedded in ARs.

2) Q_1 AND Q_2 CALCULATIONS

In the absence of direct measurements of clouds and convective systems, their thermodynamic impacts on ambient atmosphere are evaluated statistically using heat and moisture budget residuals Q_1 and Q_2 computed with the 1° $\times$ 1° YOTC analysis according to the thermodynamic and the moisture mass conservation laws. As suggested by the model trajectory study in Joos and Wernli (2012), net condensation as well as deposition contribute significantly to the total latent heating of WCBs, thus the Q_1 and Q_2 equations in Yanai et al. (1973) are modified to include the ice phase as follows (e.g., Johnson et al. 2015):

$$\begin{aligned} Q_1 &\equiv c_p\left(\frac{p}{p_0}\right)^{\kappa}\left(\frac{\partial\overline{\theta}}{\partial t}+\overline{\mathbf{v}}\cdot\nabla\overline{\theta}+\overline{\omega}\frac{\partial\overline{\theta}}{\partial p}\right)\\ &= Q_R + L_v(\overline{c}-\overline{e}) + (L_v+L_f)(\overline{d}-\overline{s}_*)\\ &\quad + L_f(\overline{f}-\overline{m}) - \nabla\cdot\overline{s'\mathbf{v}'} - \frac{\partial\overline{s'\omega'}}{\partial p}, \end{aligned} \tag{1}$$

$$\begin{aligned} Q_2 &\equiv -L_v\left(\frac{\partial\overline{q}}{\partial t}+\overline{\mathbf{v}}\cdot\nabla\overline{q}+\overline{\omega}\frac{\partial\overline{q}}{\partial p}\right)\\ &= L_v(\overline{c}-\overline{e}) + L_v(\overline{d}-\overline{s}_*)\\ &\quad + L_v\left(\nabla\cdot\overline{q'\mathbf{v}'}+\frac{\partial\overline{q'\omega'}}{\partial p}\right), \quad \text{and} \end{aligned} \tag{2}$$

$$\begin{aligned} Q_1 - Q_2 &\approx Q_R + L_f(\overline{d}-\overline{s}_*+\overline{f}-\overline{m})\\ &\quad - \left(\frac{\partial\overline{s'\omega'}}{\partial p}+L_v\frac{\partial\overline{q'\omega'}}{\partial p}\right), \end{aligned} \tag{3}$$

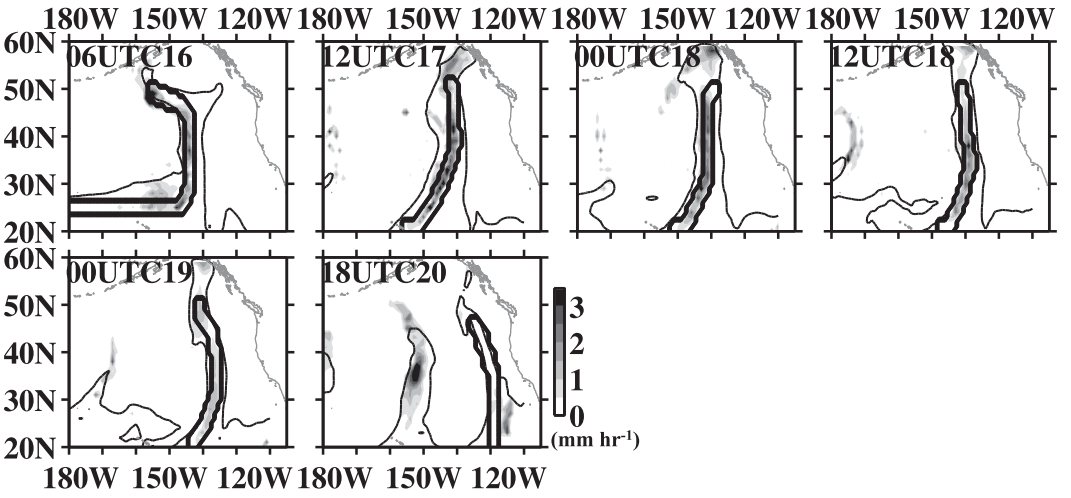

FIG. 2. As in Fig. 1, but for AR2 from 0600 UTC 16 Jan to 1800 UTC 20 Jan 2009.

where θ is the potential temperature; q is the water vapor mixing ratio; $\mathbf{v}$ is the horizontal velocity; ω is the vertical p velocity; p is the pressure; $p_0 = 1000$ hPa; $\kappa = R/c_p$ with R being the gas constant of dry air; c_p is the specific heat capacity at constant pressure; ∇ is the isobaric gradient operator; Q_R is the radiative heating rate; L_v and L_f are the latent heat of vaporization and fusion, respectively; c, e, d, s_*, f, and m are the rates of condensation, evaporation, deposition, sublimation, freezing, and melting per unit mass of air, respectively; and s is the dry static energy per unit mass of air. The overbar denotes the mean over a horizontal area equivalent to the mesh size of the gridded analysis, and the prime denotes the deviation from this mean, hence referring to subgrid-scale processes such as cloud convection, boundary layer fluxes, and turbulence. In deriving (1) and (2), the Reynolds conditions and their consequences are assumed to be accurate.

Equations (1) and (2) are calculated using the rhs of their first lines using the YOTC analysis, and are interpreted using the rhs terms in their second lines. Respectively, Q_1 represents the total effects of radiative heating, latent heat released due to microphysical phase changes, and the convergence of fluxes of sensible heat due to subgrid-scale eddies such as convection and turbulence, while Q_2 shows the total effects of net condensation and divergence of eddy moisture flux due to clouds and turbulence. In the presence of organized convection, the subgrid terms $-\partial\overline{s'\omega'}/\partial p$ and $\partial\overline{q'\omega'}/\partial p$ dominate the total eddy transports. The horizontal eddy transport terms $-\nabla\cdot\overline{s'\mathbf{v}'}$ and $\nabla\cdot\overline{q'\mathbf{v}'}$ may be ignored due to their typically small contributions (e.g., Arakawa and Schubert 1974; Wu 1994). Accordingly, the difference between Q_1 and Q_2 in (3) is indicative of net radiative heating, net latent heating associated with ice processes, and vertical eddy fluxes of moist static energy $h = s + L_v q$.

Furthermore, (1)–(3) include processes transitioning in and out of the ice phase: $\overline{d}$, $\overline{s}_*$, $\overline{f}$, and $\overline{m}$. In convective updrafts, water vapor condenses rapidly and releases latent heat. Once the environmental temperature drops below 0°C, the Bergeron process takes place; deposition outcompetes freezing and releases more latent heat. Among solid precipitation, high-density ice can survive above freezing temperatures long enough so that melting, rather than sublimation, likely contributes notably to diabatic cooling along with evaporation within downdrafts. In consequence, (1)–(3) can be approximated for convective systems as

$$Q_1 \approx Q_R + L_v(\overline{c} - \overline{e} + \overline{d}) + L_f(\overline{d} - \overline{m}) - \frac{\partial\overline{s'\omega'}}{\partial p}, \quad (4)$$

$$Q_2 \approx L_v\left(\overline{c} - \overline{e} + \overline{d} + \frac{\partial\overline{q'\omega'}}{\partial p}\right), \quad \text{and} \quad (5)$$

$$Q_1 - Q_2 \approx Q_R + L_f(\overline{d} - \overline{m}) - \frac{\partial\overline{h'\omega'}}{\partial p}. \quad (6)$$

The vertical structures of Q_1 and Q_2 that resulted from a subgrid cloud population that is predominantly deep convection are quite distinct from those that resulted from shallow convection or from convective organizations with prominent trailing stratiform clouds. Thus, the Q_1 and Q_2 profiles are commonly used to diagnose the dominant types of cloud systems (e.g., Nitta and Esbensen 1974; Houze 1989; Yanai and Johnson 1993; Tung et al. 1999; Schumacher et al. 2008). For instance, as discussed in Johnson (1984), the deep convection type exhibits net heating (positive Q_1) and drying (positive Q_2) throughout the troposphere, with a primary Q_1 peak

in the upper troposphere and a primary Q_2 peak in the lower troposphere; in contrast, the trailing stratiform type is associated with upper-tropospheric heating and drying due to condensation and deposition, and lower-tropospheric cooling and moistening contributed to by melting and evaporation of precipitation.

3) VERTICALLY INTEGRATED Q_1 AND Q_2

The vertical integrations of (4) and (5), have been widely used to determine the primary heat sources and moisture sinks (e.g., Luo and Yanai 1984; Yanai and Tomita 1998). In this study, the integrations are performed over the vertical range from $p_T = 1$ to $p_0 = 1000$ hPa, denoted by

$$\langle\ \rangle = \frac{1}{g}\int_{p_0}^{p_T} (\ )\, dp. \tag{7}$$

The difference between $\langle Q_1\rangle$ and $\langle Q_2\rangle$ might be interpreted as follows (modified after, e.g., Luo and Yanai 1984):

$$\langle Q_1\rangle - \langle Q_2\rangle \approx \langle Q_R\rangle + \langle Q_f\rangle + F_S + F_{\mathrm{LH}}, \tag{8}$$

where $\langle Q_R\rangle$, $\langle Q_f\rangle$, F_S, and F_{LH} are the column-integrated net radiative heating rate, the net heating associated with the fusion (L_f) term in (6) in the air column, the surface sensible heat flux, and the surface latent heat flux, respectively, per unit area. We further perform the spatio-temporal average (denoted by [ ]) for individual terms in (8) over various spatial domains, respectively, for the month of January, the AR1 event, and the AR2 event (see section 4c). The month of January has 124 time steps; AR1 has 19 time steps from 0000 UTC 4 January to 1200 UTC 8 January; and AR2 has 20 time steps from 0000 UTC 16 January to 1800 UTC 20 January. The $[\langle Q_1\rangle]$ and $[\langle Q_2\rangle]$ are computed from YOTC analysis. The $[\langle Q_R\rangle]$, $[F_S]$, and $[F_{\mathrm{LH}}]$ in section 5 are estimated from the YOTC forecast tendency data. This approach does not guarantee the budgets to be closed. However, as shown in section 5, the discrepancies remain one order of magnitude smaller than the leading terms.

3. Case overview

Two AR cases in January 2009 that produced intense precipitation over the west coast of North America (around 170°–110°W) are investigated (see NOAA National Climatic Data Center's State of the Climate: Global Hazards for January 2009 at http://www.ncdc.noaa.gov/sotc/hazards/2009/jan). AR1 made landfall during 4–8 January 2009. AR2 made landfall during 16–20 January 2009.

Figures 1 and 2 display the evolution of AR1 and AR2, respectively. As time elapsed, AR1 turned clockwise, and had a west–east or southwest–northeast-oriented AR1 ridge from 20° to 50°N. It made landfall from 1800 UTC 4 January to 1200 UTC 8 January (hereafter the AR1 period). Substantial oceanic precipitation was concentrated on the southwest side of AR1 (Fig. 1). In contrast, AR2 was south–north oriented roughly from 20° to 60°N. It first impacted land at 0000 UTC 16 January and left at 1800 UTC 20 January (hereafter the AR2 period). AR2 was narrower and was largely covered by enhanced precipitation (Fig. 2). In the late stages of both cases, a secondary IWV band was positioned to the west of the landfalling AR (Fig. 1 from 1200 UTC 7 January to 1200 UTC 8 January, and Fig. 2 at 1800 UTC 20 January). The secondary IWV band typically co-occurred with another cyclone (Sodemann and Stohl 2013) and would later catch up and merge with the remnants of the currently landfalling AR.

The two ARs were the most prominent cases in January 2009, which was an active month for landfalling ARs, featured by a weak La Niña condition. Figures 3 and 4 show the 200-, 500-, and 850-hPa analyses for the mean state of January 2009 and the two ARs, respectively. At 200 and 500 hPa, a ridge was located at around 135°W in the January mean state (Figs. 3a,b). At 850 hPa, a high pressure center was at 35°N, 135°W while a low pressure center was at 50°N, 170°W, with strong southwest wind in between (Fig. 3c). The 850-hPa temperature was distributed in a similar pattern as the height fields. High 850-hPa specific humidity extended northeastward from the tropics to the midlatitudes (Fig. 3d).

During the AR1 period, the 200- and 500-hPa ridges were roughly at 140°W (Figs. 4a,b), to the west of those in the January mean state (Figs. 3a,b). At 850 hPa, enhanced 850-hPa west-southwest wind was between a high pressure center at 32°N, 140°W and an elongated low pressure system, which spanned from 45°N, 158°E to 63°N, 115°W (Fig. 4c). The 850-hPa specific humidity was west–east oriented. AR1 impacted the west coast of North America from 40° to 50°N (Fig. 4d).

During the AR2 period, the 200- and 500-hPa ridges in south–north orientation were at around 122°W (Figs. 4e,f). The upper-level westerly jet split in the mid-Pacific into a northern branch into the Gulf of Alaska and a southern branch passing through Hawaii. The storm track was displaced along with the northern branch, resulting in the north–south orientation of AR2. Pronounced 850-hPa southerly winds existed in the vicinity of an 850-hPa high pressure centered at 40°N, 110°W, and a 850-hPa low pressure centered at 52°N, 175°W (Fig. 4g). Correspondingly, the 850-hPa specific humidity band was south–north oriented. AR2 impacted the west coast of North America

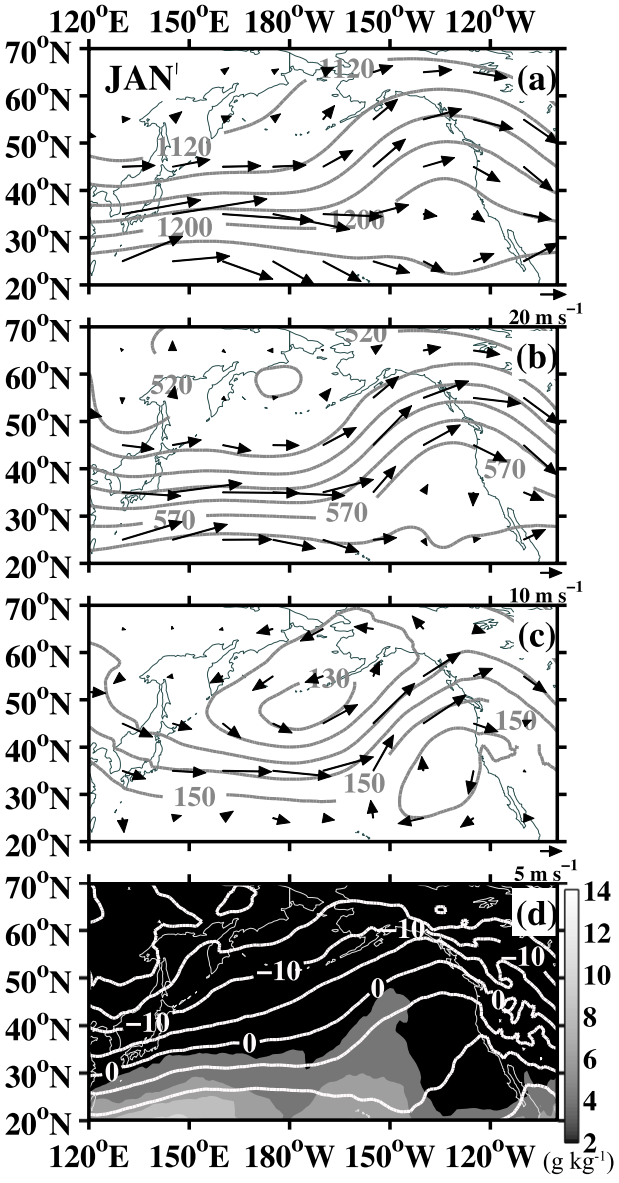

FIG. 3. Mean states for January 2009: (a)–(c) 200-, 500-, and 850-hPa wind vectors (m s^{-1}) and height contours with intervals of 20, 10, and 5 dam, respectively. (d) The 850-hPa temperature (contour intervals of 5°C) and specific humidity (shading intervals of 2 g kg^{-1}).

from 55° to 60°N (Fig. 4h). It was narrower and shorter than its counterpart in the AR1 period.

The accumulated GPCP precipitation is illustrated in Fig. 5. AR1 had a broad precipitation band in a nearly west–east orientation. It made landfall in the province of British Columbia in Canada and the states of Washington and Oregon in the United States. AR2 had a narrow precipitation band in a south–north orientation. It penetrated inland Alaska and British Columbia. A comparison between specific humidity (Figs. 4d,h) and precipitation (Fig. 5) indicates that the likelihood of precipitation can be predicted from the high specific humidity content, especially over the midlatitude ocean. Over the ocean, accumulated precipitation with values ≥40 mm was mainly scattered on the southwest and northeast sides of AR1, whereas it was distributed continuously along the main path of AR2. In both ARs, precipitation was stronger in the landfalling regions than that over the ocean.

The large-scale convergence induced by merging multiple high IWV bands can increase the moisture content of an AR (e.g., Ralph et al. 2004; Bao et al. 2006). This process is often associated with multiple eastward-propagating cyclones (Cordeira et al. 2013; Sodemann and Stohl 2013). Clearly, the main merging location for AR1 was around 20°–35°N, 180°–165°W (the first two rows in Fig. 6a). In contrast, the location for AR2 extended to higher latitudes centered at 28°–50°N, 160°–140°W (the first row in Fig. 7a). After merging, the saturated and actual vapor pressures in the lower troposphere were largely enhanced. Figure 8 depicts the differences in saturated vapor pressure of 2-m air between the AR periods and the no-AR period. The latter period is computed by excluding time steps in AR1 and AR2 periods from January 2009. Qualitatively similar features are observed for both ARs. First, positive saturated vapor pressure was mostly present inside the enhanced IWV bands. Second, the local maxima of saturated vapor pressure were situated near the merging locations (Figs. 6–8), mostly outside of the maximum precipitation centers (Figs. 8 and 5). The positive differences imply an increase of the maximum possible amount of moisture that can exist in the lower-tropospheric air, owning to the conveyance and confluence of warm air by the ARs.

The merging process amplifies precipitation, which consumes moisture as well as releases latent heat in an AR. Figures 6b and 7b present the average vertical profiles between 30° and 35°N for wind, specific humidity, and positive Q_1 for AR1 and AR2, respectively. Black and gray arrows mark the locations of the primary specific humidity peaks and the secondary specific humidity peaks, respectively. The peaks are in correspondence with the IWV bands in Figs. 6a and 7a. For AR1 at 0600 UTC 2 January, the primary specific humidity peak was located from 160°E to 170°W. The secondary specific humidity peak was at around 165°W. The Q_1 maximum was at around 170°E, 500–700 hPa, coinciding with substantial upward motions (the first row in Fig. 6b). As the high IWV bands merged and proceeded eastward, the primary specific humidity peak became narrower, and the associated heating intensified (the second and the third rows in Fig. 6). At 0600 UTC 5 January, the specific humidity peak was at 170°W, with a weakening heating center (the fourth row in Fig. 6b). At 0600 UTC 6 January, the specific

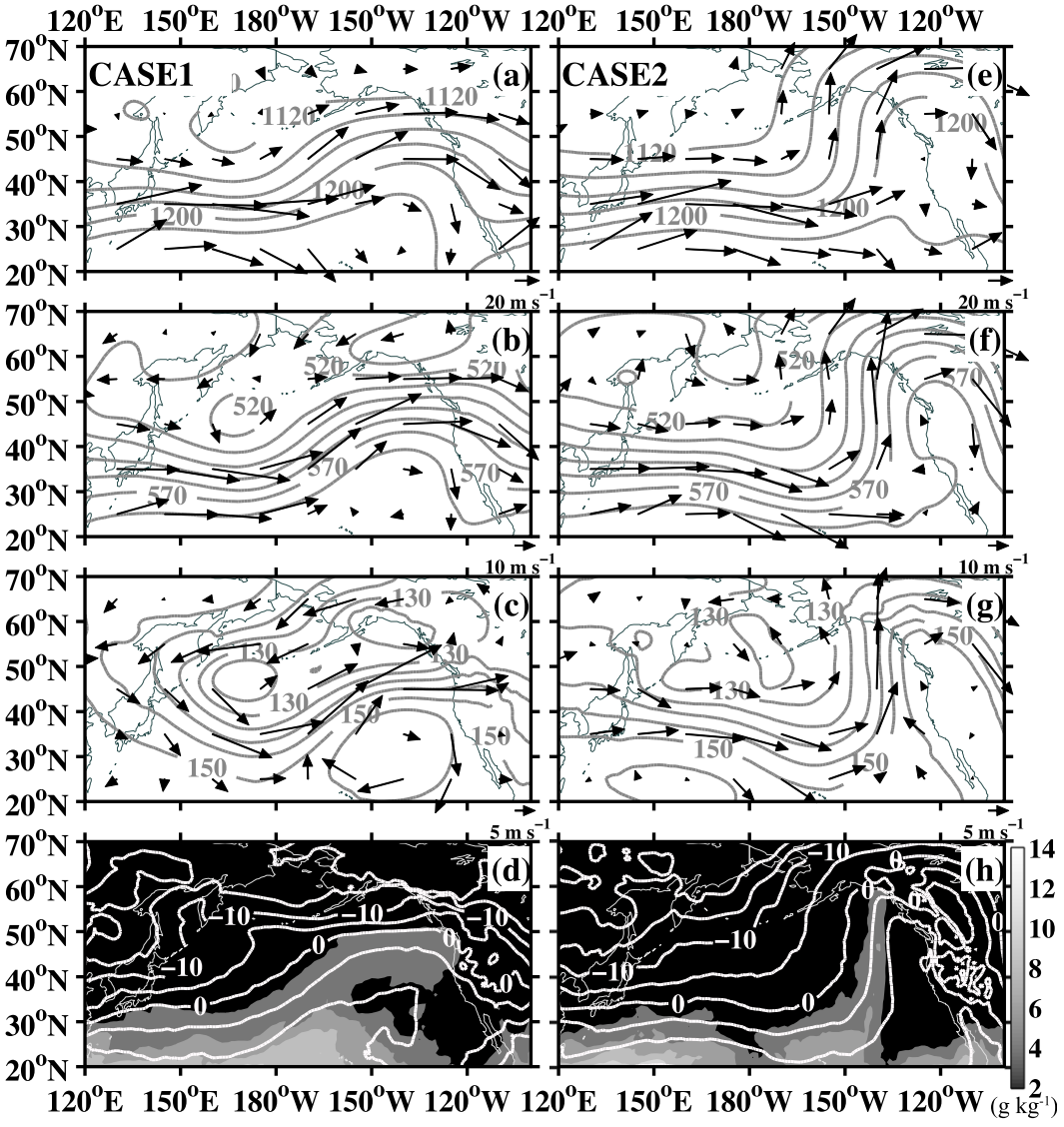

FIG. 4. As in Fig. 3, but for (left) AR1 and (right) AR2.

humidity peak propagated to around 160°W, while the Q_1 maximum became hard to discern (the last row in Fig. 6b). For all time steps in Fig. 6b, strong westerlies were present to the west of the primary specific humidity peaks, in contrast to the weak wind to the east of the primary specific humidity peaks. A similar evolution is observed in AR2 (Fig. 7b). However, the primary specific humidity peak was narrower than that in AR1.

4. Precipitating convection

a. Along-AR propagation

Figures 9 and 10 depict Q_1, $Q_1 - Q_2$, and CMORPH precipitation along the AR ridges from the southwest end to the northeast end. They are taken at time steps identical with those in Fig. 1 for AR1 and overlapped with those in Fig. 2 for AR2. The x axis is the distance from the southwest end. As a reference for the spatial progression of the AR1 ridge, three vertical lines are drawn to show where AR1 intersected longitudes at 165°, 153°, and 141°W, respectively. For the mainly north–south-oriented AR2, the vertical lines are for latitudes at 25°, 35°, and 45°N, respectively. The tropopause was around 200 hPa in the AR1 ridge, and was around 300 hPa in the AR2 ridge (indicated by 1.5×10^{-6} K kg^{-1} m^2 s^{-1} or 1.5 PVU, not shown). The different tropopause heights between the two ARs were likely resulted from their different latitudinal ranges.

The precipitating systems in AR1 underwent two distinct phases of development characterized by heating

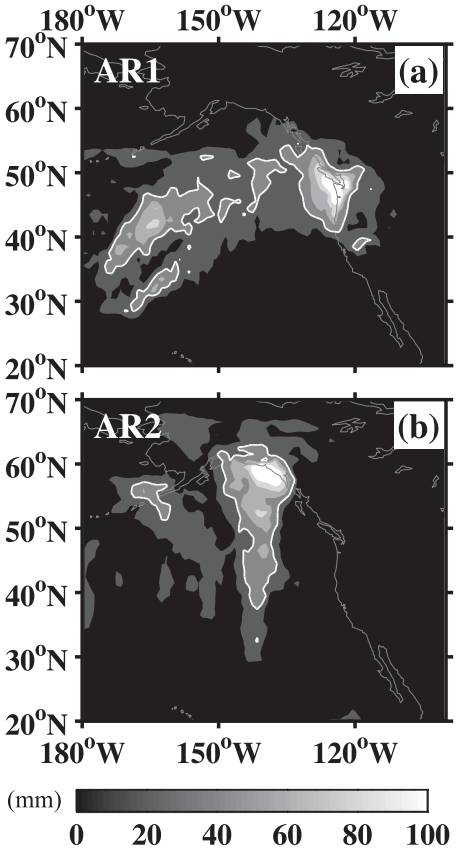

FIG. 5. The 4-day accumulated GPCP daily precipitation (shading intervals of 20 mm, white contour denotes 40 mm): (a) AR1 from 4 to 8 Jan 2009 and (b) AR2 from 16 to 20 Jan 2009.

(Q_1) profiles, which are described as strengthening and weakening phases as follows. Figures 9a–e show the strengthening phase of the precipitating systems in AR1. The system appears to be composed of two convective organizations, each with a spatial scale around 2000 km horizontally, evolving from vertical to tilted structures in roughly two days. At 0000 UTC 4 January (Fig. 9a), a 400–900-hPa heating with $Q_1 \geq 15\,\mathrm{K\,day^{-1}}$ emerged at 30°–35°N, 180°–175°W. Maximum heating was near 500 hPa. Cooling existed below 950 hPa. At 1800 UTC 4 January (Fig. 9b), the heating became elongated and vertically tilted from 25°N, 180° to 40°N, 166°W. Its west part exhibited net heating from 300 to 900 hPa. Its east part exhibited a mature mesoscale convective system type of upper-tropospheric heating (maximized near 450 hPa) and lower-tropospheric cooling (peaked at 800 hPa). At 0600 UTC 5 January (Fig. 9c), heating expanded eastward to 30°–40°N, 178°–160°W. At 1800 UTC 5 January, another system started, apparently mixed with shallower and deep convection types (left column of Fig. 9d), producing localized intensive precipitation up to $3\,\mathrm{mm\,h^{-1}}$ at 29°–36°N (right column of Fig. 9d). At 1800 UTC 6 January (Fig. 9e), an obvious tilted heating was at 26°–44°N, 162°–147°W. The tilting tendency, again, implies a transition of dominant cloud types from shallower convection on the west side to deeper convection and trailing stratiform on the east side.

Figures 9f and 9g are considered the weakening phases of the AR1 precipitating systems. The precipitating system propagated eastward and subsided (Figs. 9f,g), and its remnants produced less than $30\,\mathrm{K\,day^{-1}}$ of Q_1 at 1200 and 1800 UTC 7 January. The Q_1 maxima were largely confined below 600 hPa. The strong Q_1 signals at the east end of the AR1 ridge (e.g., Fig. 9f) were produced by the landfalling precipitating systems; hence, they are not discussed here.

The precipitating systems in AR2 covered a large fraction of the AR ridge, which was, however, shorter than that of AR1 (see Figs. 9 and 10). In the strengthening phase of AR2 at 1200 UTC 17 January (Fig. 10a), the primary heating with $Q_1 \geq 15\,\mathrm{K\,day^{-1}}$ was to the south of 45°N from 400 to 900 hPa. It was vertically tilted over a horizontal distance around 2000 km, similar in structure and scale to the system in AR1. The entire precipitating systems strengthened and propagated northward, and at 0000 UTC 18 January (Fig. 10b), the heating center expanded from 23°N, 145°W to 48°N, 141°W. The tilt of Q_1 is suggestive of dominant cloud types transitioning from shallower to deep convection with trailing stratiform; however, it was not as pronounced a feature here as in AR1. In the weakening phase of AR2, precipitating systems still covered a substantial portion of the AR2 ridge (Fig. 10c at 1200 UTC 18 January and Fig. 10d at 0000 UTC 19 January).

The vertical profiles of $Q_1 - Q_2$ appear to be complicated juxtapositions of latent heating and eddy transports associated with various cloud types. Equation (6) provides simplified guidelines to understand the $Q_1 - Q_2$ maps. The variable Q_R in the troposphere tends to be on the order of $-1\,\mathrm{K\,day^{-1}}$. A pronounced feature in these maps is a dipole of a negative center immediately below a positive center. There can be two sets of dipoles stacked vertically in the low to midtroposphere, such as around 1500 km in Fig. 9b, around 1000 km in Fig. 9c, and between 1000 and 3000 km in Figs. 10a–c. These dipoles indicate divergence of moist static energy h at the lower level and convergence at the upper level, which support strong evidence of vertical transport of moist static energy via convection. The two stacked dipoles are suggestive of the presence of at least two dominant convection cloud types detraining at different heights. Shallow cumulus and stratiform systems lack such a transport mechanism, hence, they tend to yield a vertically uniform $Q_1 - Q_2$ field. However, the trailing stratiform may be associated with a center of depositional

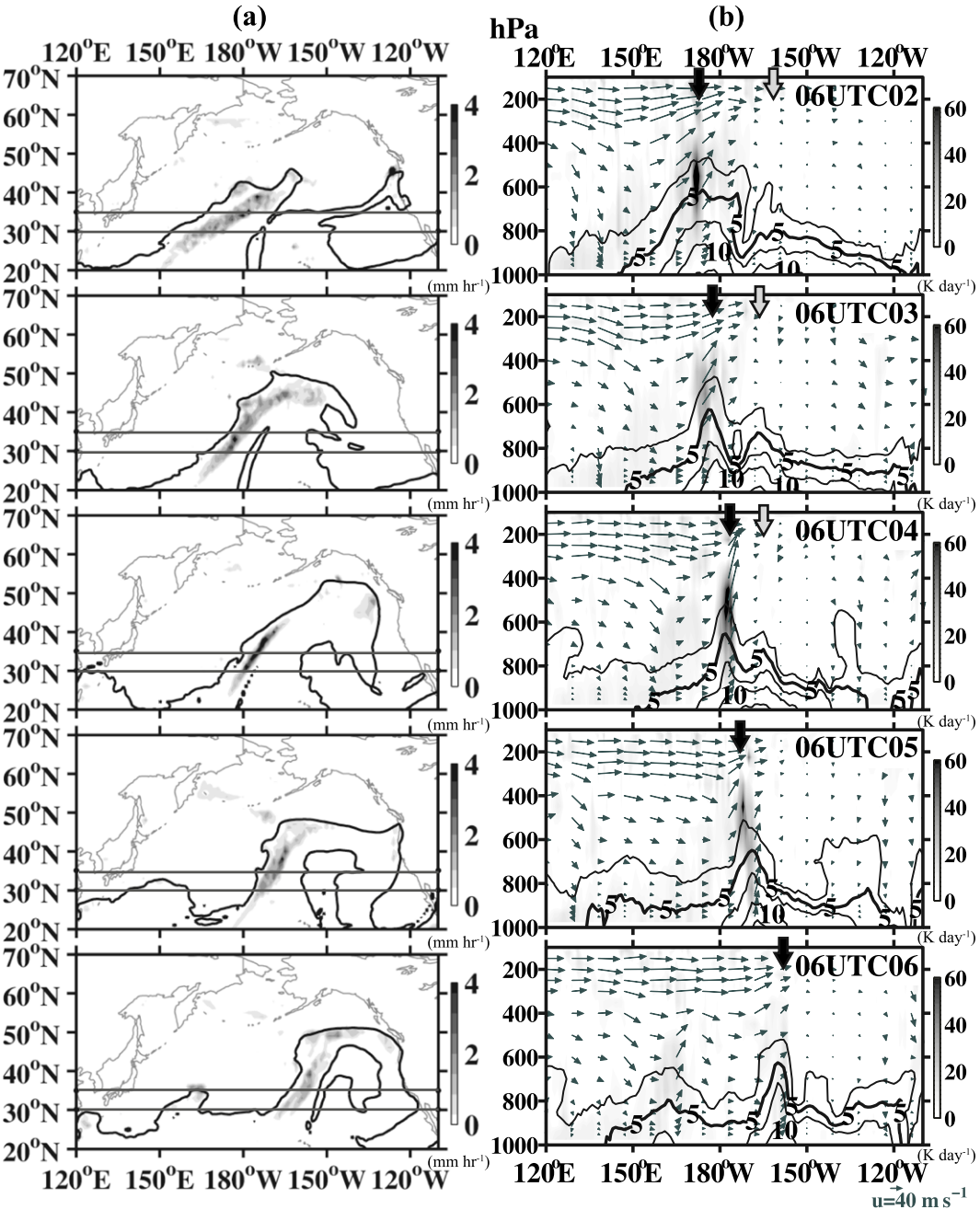

FIG. 6. Merging process for AR1 from 0600 UTC 2 Jan to 0600 UTC 6 Jan 2009: (a) in a plan view, CMORPH precipitation in mm h^{-1} is shaded, IWV = 20 mm is the thick contour, 30° and 35°N are marked by horizontal lines; (b) in a vertical section averaged over 30°–35°N for u, ω vectors (u in m s^{-1} and ω in 10^{-2} Pa s^{-1}), specific humidity with contour intervals of 2.5 g kg^{-1}, and positive Q_1 (shades, K day^{-1}). Black and gray arrows denote the primary and secondary specific humidity peaks, respectively.

heating above the freezing level and melting cooling around the freezing level, according to (6). The depositional heating–melting cooling might have enhanced the dipoles between 400 and 800 hPa at 1500 km in Fig. 9b, at 1000 km in Fig. 9c, and at 3000 km in Fig. 10b. Last, under the undisturbed condition, the typical mixed layer turbulent mixing results in convergence of heat and moisture, hence, positive $Q_1 - Q_2 - Q_R$ in the PBL. Examples can be seen in the narrow positive zones in the lowermost troposphere in Figs. 9f and 9g.

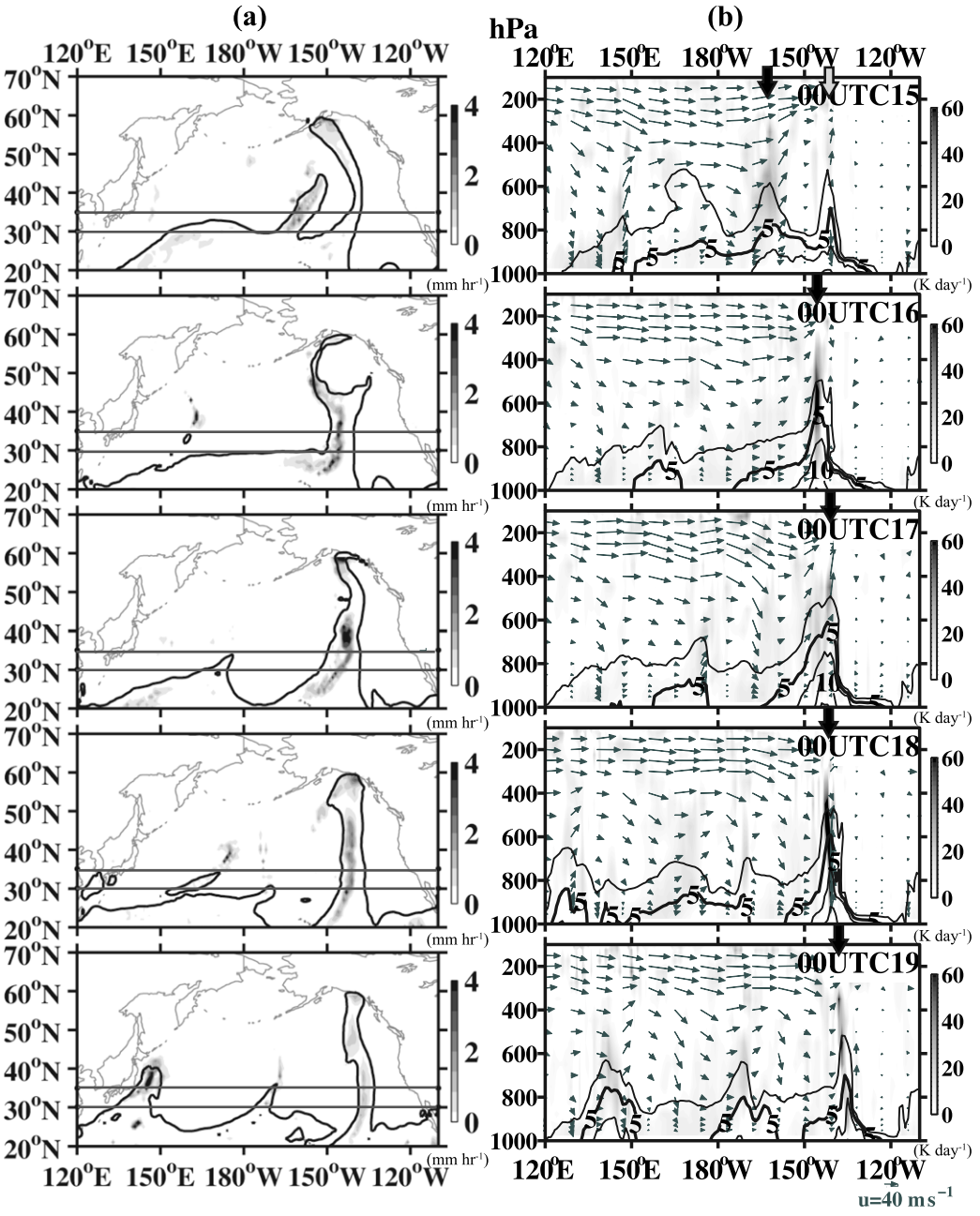

FIG. 7. As in Fig. 6, but for AR2 from 0000 UTC 15 Jan to 0000 UTC 19 Jan 2009.

In the weakening phase, AR2 did not exhibit the shallower-convection-dominant heating profile as AR1 did in Figs. 9f and 9g. This and the large precipitating convection coverage of the short AR2 ridge differentiate the two AR events. Considering that the precipitating convective organizations in both ARs developed to a similar spatial scale, one may conjecture that these systems drew moisture from the moisture reservoir in the tropics and depleted most of it on the spot. For AR1 to deliver moisture and make an impact upon landfall at a farther downstream location, extratropical heat and moisture sources must have been tapped into; therefore, the significant shallower cloud types and PBL mixing took place at its later stage.

b. *Average Q_1 and Q_2 profiles*

In Figs. 11 and 12, we conduct multiscale comparisons of the Q_1 and Q_2 inside the precipitating areas within the

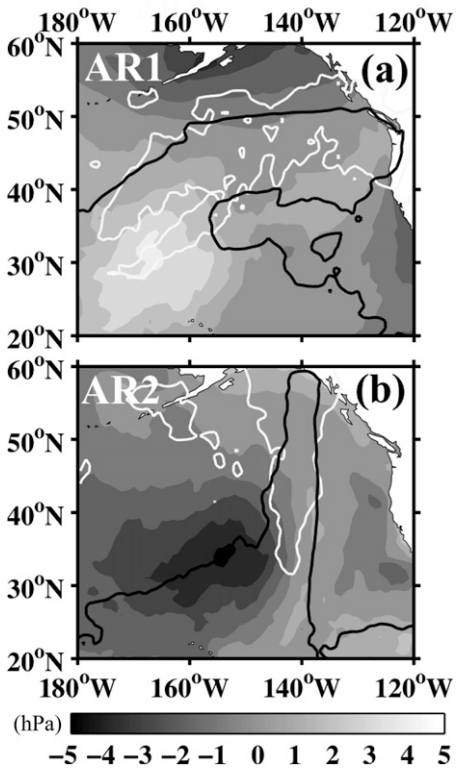

FIG. 8. Differences in saturated vapor pressure of 2-m air between the AR and no-AR periods (January 2009 excluding time steps during AR1 and AR2 periods) are shaded, with 2-hPa intervals: (a) AR1 and (b) AR2. White contours are 4-day accumulated GPCP precipitation = 30 mm. Black contours are temporal averaged 850-hPa specific humidity = 4 g kg^{-1}.

AR ridges, inside the AR-IWV, and outside the AR-IWV in the NE Pacific region. Figure 11 illustrates the average Q_1 and Q_2 profiles for the precipitating systems only in the AR ridge (hereafter the precipitating AR ridge) at selected time steps. During the strengthening phase of precipitating systems in the AR1 ridge (Fig. 11a), a transition from the deep convection type of low- to midtropospheric heating and drying (e.g., 0600 and 1200 UTC 4 January) to the stratiform dominant type of midtropospheric heating and drying is observed (~550 hPa at 1800 UTC 4 January, see Johnson 1984; Houze 2004; Schumacher et al. 2008). However, the stratiform type of midtropospheric heating and drying quickly weakened. During the weakening stage (Fig. 11b), the main heating and drying peak shifted to around 800 hPa (e.g., 1800 UTC 6 January, 1200–1800 UTC 7 January). This indicates the existence of low-level clouds, and the weakening of convective transport. On the contrary, the precipitating AR2 ridge had a robust deep convection type of heating throughout the strengthening phase. For example, at 1800 UTC 16 January–0600 UTC 17 January in Fig. 11c, the Q_1 and Q_2 extrema clearly separated, suggesting the presence of eddy vertical transport of moist static energy. Strong heating and drying remained prominent in the third landfall day of AR2 (e.g., 1200 UTC 18 January in Fig. 11d). The primary Q_1 peak was between 550 and 650 hPa, and the Q_2 peak was around 650 hPa during the weakening phase (Fig. 11d), implying the abundance of midtropospheric clouds. Notice that Q_1 profiles above 300 hPa in AR1 (Figs. 11a,b) and above 400 hPa in AR2 (Figs. 11c,d) are likely around and above the tropopause. The budget residuals are subjected to erroneous values arising from small perturbations in vertical velocity multiplied with a vertical temperature gradient under large static stability. The variations seen above these levels are therefore not interpreted.

Figure 12 compares the Q_{1I} (dark lines) and $(Q_1 - Q_2)_I$ (dark dashed lines) profiles for the AR-IWV average over the AR1 and AR2 periods. Recall that even though both AR ridges contained precipitating convective organizations, the one in the AR1 ridge was overtaken by shallower convection at its later stage prior to landfall. So, we anticipate that on average heating and drying associated with deep convective systems affected AR1-IWV less than AR2-IWV. Indeed, such a difference is observed. As seen in Fig. 12a, negative $(Q_1 - Q_2)_I$ was present throughout most of the troposphere above 900 hPa in AR1-IWV, which could be largely explained by radiative cooling. In contrast, a double-peak structure of $(Q_1 - Q_2)_I$ was present in AR2-IWV, along with an overall stronger low- to midtropospheric positive Q_{1I} (Fig. 12b). As discussed in section 4a, the double-peak profile of $(Q_1 - Q_2)_I$ is likely the manifestation of vertical transports of moist static energy associated with convection detraining at different heights, overlaid with signals of depositional heating between 400 and 600 hPa and melting cooling around 600 hPa associated with a stratiform anvil.

Outside AR-IWV, large-scale downward motion largely dominated (not shown), along with heating (Q_{1O} in Figs. 12a,b) and moistening due to PBL turbulence mixing, and minor midtropospheric drying in both ARs. However, the depth of the low-level heating and moistening was different between the two cases. The Q_{1O} profile for the AR1 period (Fig. 12a) exhibits heating below 900 hPa and cooling between 400 and 900 hPa, with a heating maximum of 3 K day^{-1} near the surface. Positive $(Q_1 - Q_2)_O$ existed below 750 hPa due to the prominent moistening in these levels. In contrast, a deeper layer of near-surface heating and moistening is observed during AR2, peaking at around 900 hPa (Fig. 12b). Moreover, radiative cooling dominated the heating profile above 800 hPa in the AR1 period (Fig. 12a), yet its impact seems to be offset by other sources of heating during the AR2 period (Fig. 12b).

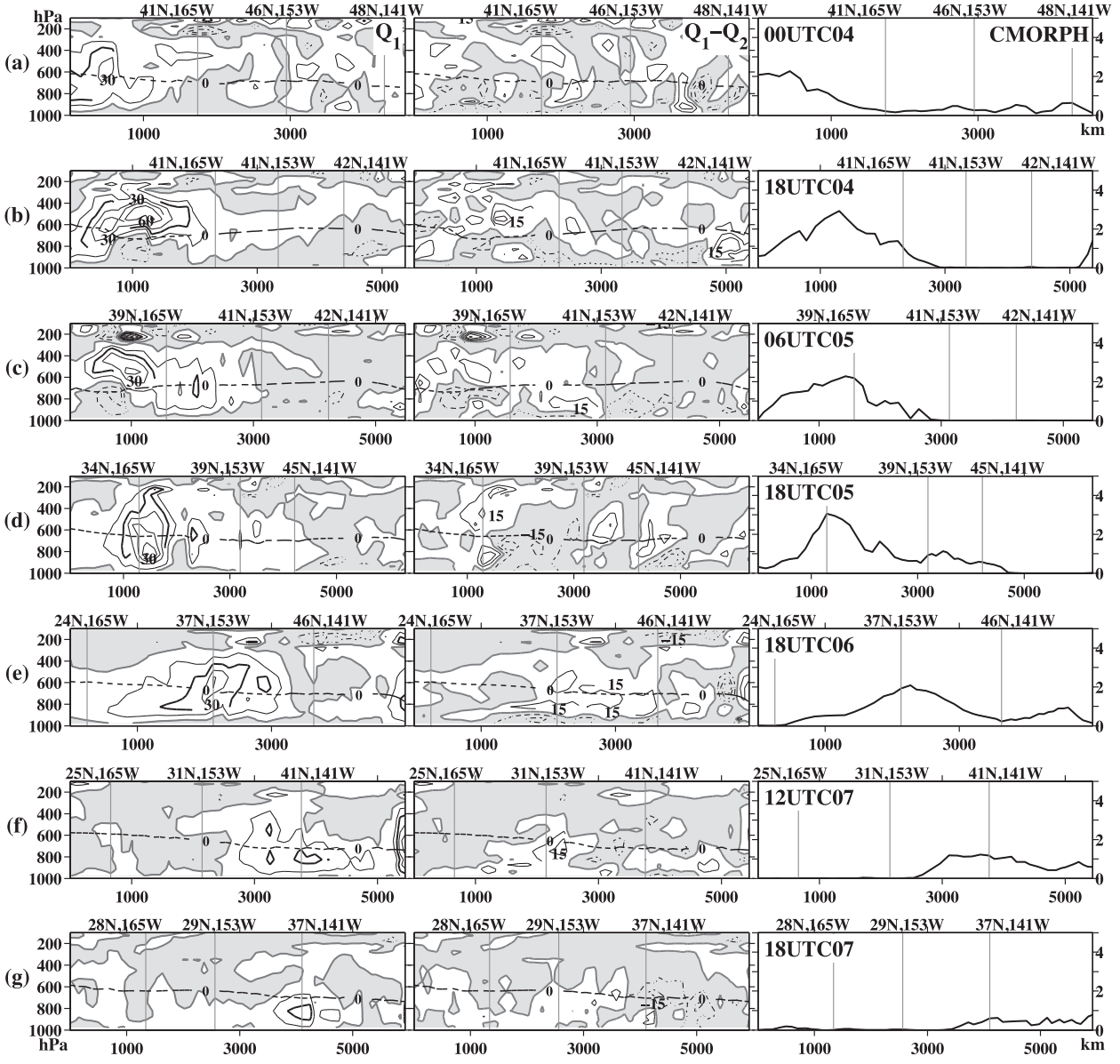

FIG. 9. Vertical sections along the AR1 ridge plotted from 0000 UTC 4 Jan to 1800 UTC 7 Jan 2009 for (left) Q_1 (K day^{-1}), (center) $Q_1 - Q_2$ (K day^{-1}), and (right) CMORPH precipitation (mm h^{-1}); Q_1 and $Q_1 - Q_2$ are in contours with 15 K day^{-1} intervals, with negative values shaded. Horizontal dashed lines mark the temperature at 0°C. The top x axis marks the coordinates where the AR1 ridge intersected at 165°, 153°, and 141°W. The bottom x axis is distance (km). The y axes for Q_1 and $Q_1 - Q_2$ are pressure (hPa).

c. *Vertically integrated Q_1 and Q_2*

To yield insights into the net impacts of subgrid-scale processes on the surrounding environment, we compare $\langle Q_1 \rangle$, $\langle Q_2 \rangle$, $\langle Q_R \rangle$, F_{LH}, and F_S averaged over the NE Pacific region, AR-IWV, outside AR-IWV, and the precipitating AR ridges during the January, AR1, and AR2 periods (Tables 1 and 2). To highlight results from the lhs of (8) in Table 1, Fig. 13 shows the spatiotemporal average $\langle Q_1 \rangle$ and $-\langle Q_2 \rangle$ from YOTC analysis. The atmosphere over the NE Pacific was subjugated to a heat sink (negative spatiotemporal average $\langle Q_1 \rangle$, hereafter, $[\langle Q_1 \rangle]$) and moisture sink (positive $[\langle Q_2 \rangle]$) during the January and AR1 periods (Table 1), suggesting the importance of radiative cooling. However, it was a heat source and moisture sink in the AR2 period, implying the importance of latent heating and surface evaporation.

Meanwhile, weaker upwelling $[F_{LH}]$ and $[F_S]$ are found in the AR1 period than in the AR2 period for all regions (Table 2 and Fig. 14), even though AR1 and

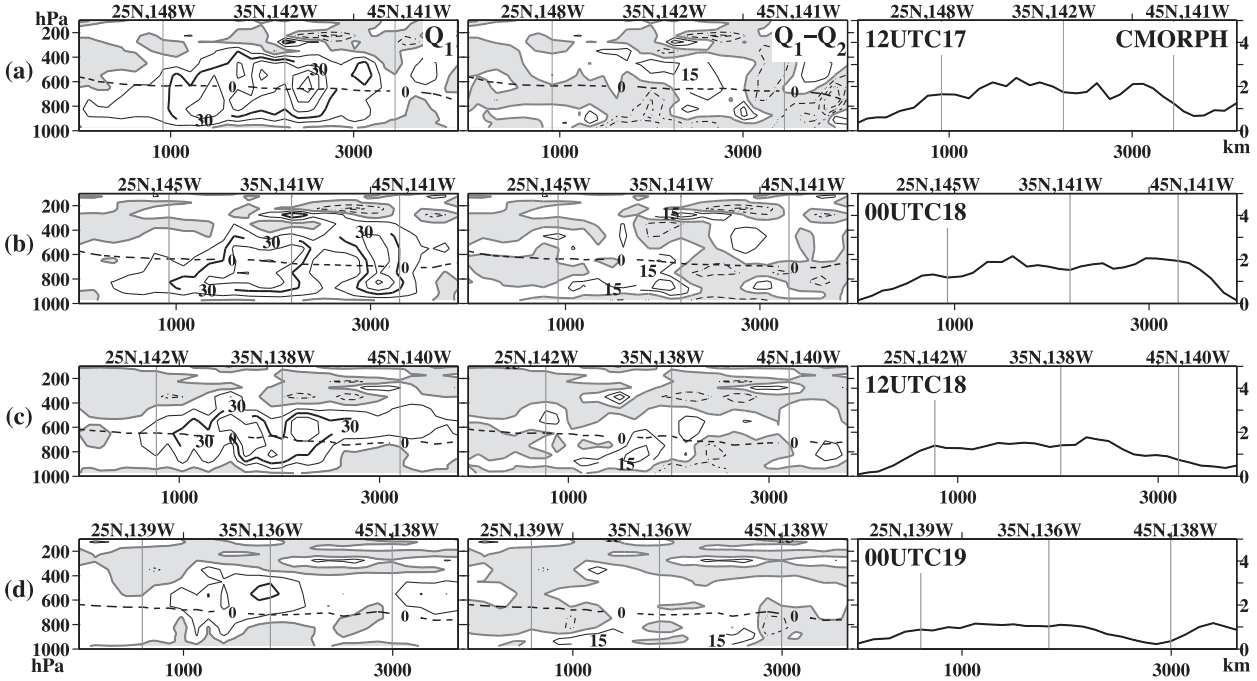

FIG. 10. As in Fig. 9, but for the AR2 ridge plotted from 1200 UTC 17 Jan to 0000 UTC 19 Jan 2009. Three vertical lines mark where the AR2 ridge intersected at 25°, 35°, and 45°N.

AR2 had comparable near-surface wind speed (not shown). Such a contrast amplified in IWV, with downward $[F_S]$ being observed in AR1-IWV. These suggest that the near-surface air in AR1-IWV was excessively warm and moist. In fact, calculations from YOTC analysis show that the mean temperature of 2-m air was 0.61°C higher than that of the sea surface in the precipitating AR1 ridge. Moreover, the differences in actual vapor pressure between 2-m air and the sea surface were smaller in the precipitating AR1 ridge than those in the outside domains (not shown). Presumably, the downward $[F_S]$ and weak upwelling $[F_{LH}]$ in AR1-IWV are related to the lack of strong and persistent convection. Therefore, the warm air mass in AR1 was

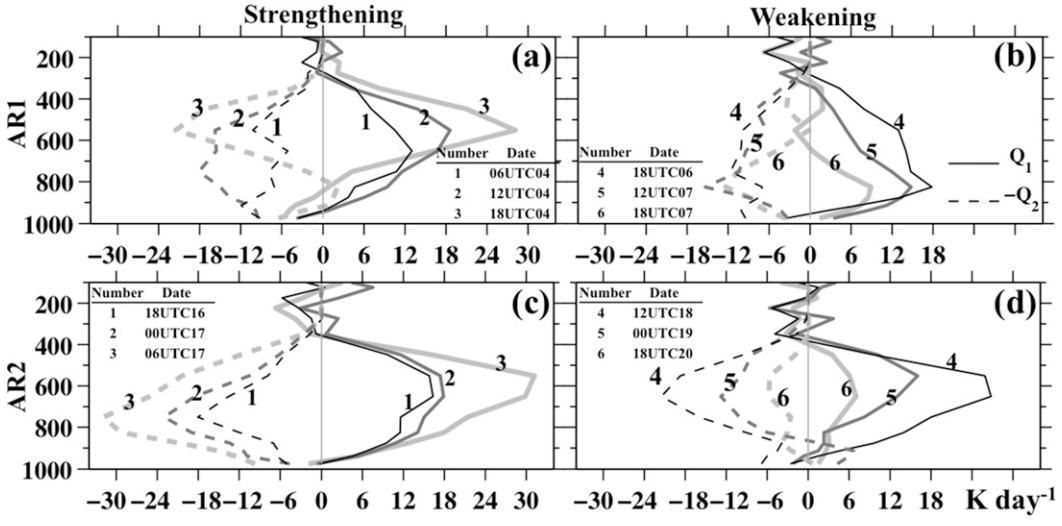

FIG. 11. Vertical profiles averaged over the precipitating AR ridges: lines are Q_1 and dashed lines are $-Q_2$. (a),(c) Lines 1–3 are the strengthening time steps in AR1 or AR2. (b),(d) Lines 4–6 are the weakening phase of AR1 or AR2. The x axis is the amplitude of Q_1 and $-Q_2$ (K day^{-1}) and the y axis is the pressure (hPa).

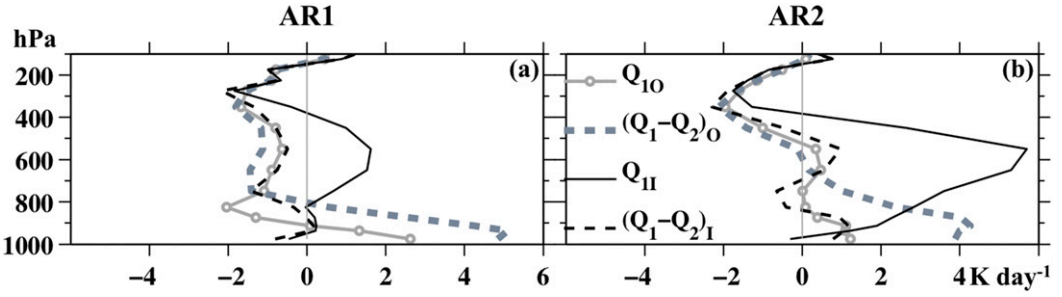

FIG. 12. Average vertical profiles during the (a) AR1 and (b) AR2 periods. Dark lines {light lines with circles} are Q_1 inside {outside} AR-IWV, denoted as Q_{1I} $\{Q_{1O}\}$. Dark {light} dashed lines are $Q_1 - Q_2$ inside {outside} AR-IWV, denoted as $(Q_1 - Q_2)_I$ $\{(Q_1 - Q_2)_O\}$. Vertical lines mark the 0 values. The x axis is the amplitude (K day^{-1}) and the y axis is the pressure (hPa).

able to retain a large amount of moisture in propagation. In addition, the reevaporation of precipitation under stratiform cloud decks likely served as an extra moisture source for the near-surface air (sections 4a and 4b). In brief, precipitating systems in ARs appeared to play a crucial role in modifying the heat and moisture budget as well as air–sea interactions in ARs.

d. *CRF implications*

Table 3 shows the shortwave cloud forcing ($C_s = S_{\text{clr}} - S_{\text{cld}}$, where S_{clr} is the clear-sky reflected shortwave radiation, and S_{cld} is the cloudy-sky reflected shortwave radiation), longwave cloud forcing ($C_l = \text{OLR}_{\text{clr}} - \text{OLR}_{\text{cld}}$, where OLR is the outgoing longwave radiation), and cloud radiative forcing ($\text{CRF} = C_s + C_l$) averaged over AR1 and AR2 periods (see Ramanathan et al. 1989). Notice that 1800 UTC 20 January is omitted, so that both ARs have 10 time steps for local morning and 9 time steps for local evening.

The spatiotemporal average CRF or [CRF], is negative over all domains, an indication of the net cloud radiative cooling effect on the surface–atmosphere system. Moreover, AR1 had less [CRF] ($-18.3\,\text{W m}^{-1}$) in AR-IWV than AR2 ($-32.9\,\text{W m}^{-1}$). Such a contrast was amplified in the precipitating AR ridge. This is mainly because clouds in AR2-IWV had a stronger shortwave reflection at the top of atmosphere (more negative [C_s]) than those in AR1-IWV. In addition, clouds in the AR2 ridge exhibited slightly weaker longwave forcing ([C_l]) than those in the AR1 ridge. As discussed in section 4a, the AR2 ridge had relatively more strong convection and a lower tropopause, with a strong heating center being confined below 400 hPa (Figs. 10a,b). Hence, clouds in AR2 were highly reflective. They effectively blocked the shortwave radiation from arriving the surface (not shown), and emitted more [OLR] than in AR1. On the contrary, the AR1 ridge had less coverage of strong convection with a higher tropopause. Thus, convection in AR1 was able to develop to higher altitudes (e.g., the west-end heating center with $Q_1 \geq 30\,\text{K day}^{-1}$ reached upward to approximately 350 hPa in Figs. 9b,c), and likely retained more longwave radiation in the atmosphere.

5. Discussion

Three interesting observations had been made in this study. First, large-scale convergence through merging sequential IWV bands over the ocean increased the temperature and moisture content of the newly formed AR. The conveyance and confluence of warm air in this process appeared to enhance the saturated vapor pressure or the maximum possible amount of moisture that can exist in lower-tropospheric air. Such a process, presumably, enhances the moisture transport effectiveness by an AR. Second, precipitating systems associated with convergences and frontal lifting mainly acted to deplete the moisture from and release latent heat in the AR. This underlines the importance of subgrid-scale processes in the maintenance and landfalling impacts of an AR. Third, the precipitating systems in AR often revealed a vertically tilted structure, suggesting the existence of various kinds of convection from shallower

TABLE 1. [$\langle Q_1 \rangle$] and [$\langle Q_2 \rangle$] (W m^{-2}) averaged over the NE Pacific region, AR-IWV, outside AR-IWV, and the precipitating AR ridge for January, AR1, and AR2 periods.

		Jan	AR1	AR2
[$\langle Q_1 \rangle$]	NE Pacific	−11.9	−29.1	18.0
	AR-IWV	148.7	41.9	201.7
	Outside AR-IWV	−79.8	−86.9	−47.9
	Precipitating AR ridge	—	624.7	709.9
[$\langle Q_2 \rangle$]	NE Pacific	12.3	27.3	14.0
	AR-IWV	177.2	121.3	236.9
	Outside AR-IWV	−59.2	−52.5	−65.4
	Precipitating AR ridge	—	724.7	770.9

TABLE 2. As in Table 1, but for $[\langle Q_R \rangle]$, $[F_{LH}]$, $[F_S]$, and $([\langle Q_1 \rangle] - [\langle Q_2 \rangle]) - ([\langle Q_R \rangle] + [F_{LH}] + [F_S])$ (W m^{-2}).

		Jan	AR1	AR2
$[\langle Q_R \rangle]$	NE Pacific	−135.5	−147.1	−131.7
	AR-IWV	−132.8	−148.7	−139.0
	Outside AR-IWV	−136.0	−145.8	−129.1
	Precipitating AR ridge	—	−136.9	−137.0
$[F_{LH}]$	NE Pacific	103.9	91.6	128.9
	AR-IWV	98.3	79.0	109.7
	Outside AR-IWV	107.0	103.8	109.8
	Precipitating AR ridge	—	9.6	51.8
$[F_S]$	NE Pacific	20.5	17.1	30.4
	AR-IWV	6.1	−1.3	10.7
	Outside AR-IWV	27.9	33.0	37.6
	Precipitating AR ridge	—	−17.5	2.5
$([\langle Q_1 \rangle] - [\langle Q_2 \rangle]) - ([\langle Q_R \rangle] + [F_{LH}] + [F_S])$	NE Pacific	−13.3	−18.0	−23.6
	AR-IWV	0.0	−8.4	−16.6
	Outside AR-IWV	−19.5	−25.4	−0.8
	Precipitating AR ridge	—	44.8	21.7

ones, to deep convection, and to the trailing stratiform deck. The variations in spatial coverage and cloud types could translate to differences in radiative forcing and surface heat fluxes, thus affecting regional heat and moisture balance.

This work emphasizes the significance of precipitating convection inside ARs. Four questions can be asked based on the results. First, from a statistical point of view, what are the impacts of the subgrid-scale processes on air–sea interactions and on the heat balance in extratropics? Second, how do variations in the abundance and types of convection translate to climate-scale CRF variability? Third, how do subgrid-scale processes affect moisture sources and perhaps the intensity of landfalling precipitation of the ARs? As implied by our study, precipitating convection appears to remove moisture

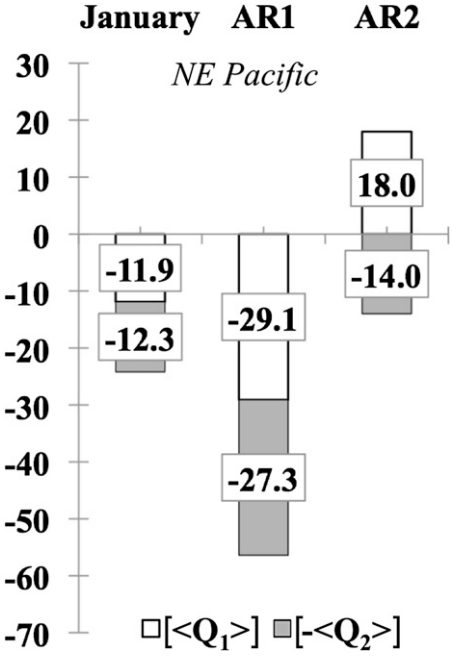

FIG. 13. Spatiotemporal average $\langle Q_1 \rangle$ and $-\langle Q_2 \rangle$ for the NE Pacific region in W m^{-2}.

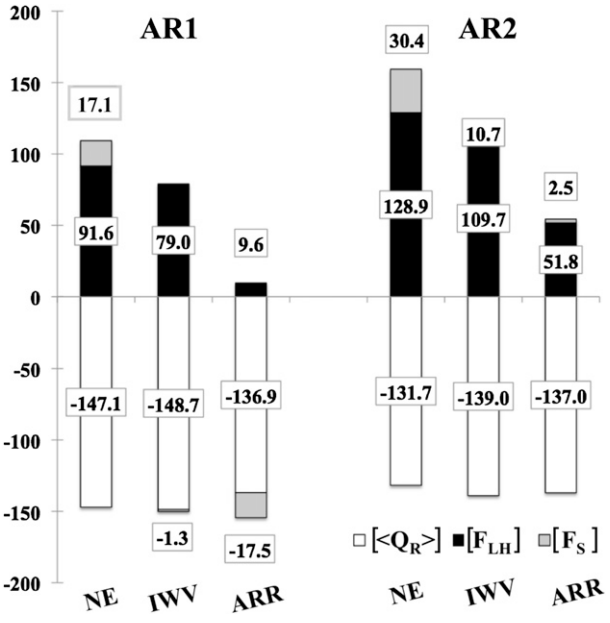

FIG. 14. Spatiotemporal average upward F_S, upward F_{LH}, and $\langle Q_R \rangle$ (W m^{-2}) for the NE Pacific region (NE), AR-IWV (IWV), and the precipitating AR ridge (ARR) for AR1 and AR2.

TABLE 3. As in Table 1, but for [C_s], [C_l], [OLR], and [CRF] (W m^{-2}) during the AR1 and AR2 periods.

	AR1				AR2			
	NE Pacific	AR-IWV	Outside AR-IWV	Precipitating AR ridge	NE Pacific	AR-IWV	Outside AR-IWV	Precipitating AR ridge
[C_s]	−41.7	−51.4	−33.5	−67.3	−38.9	−69.7	−27.1	−92.7
[C_l]	25.7	33.0	19.5	63.8	24.3	36.8	19.8	55.7
[OLR]	238.2	239.9	237.4	192.7	241.9	240.1	242.3	214.9
[CRF]	−16.0	−18.3	−14.0	−3.5	−14.6	−32.9	−7.4	−37.0

from distant tropical regions; meanwhile, it seems to introduce localized moisture sources to the ARs via precipitation reevaporation and, to a lesser degree, evaporation from the sea surface. Fourth, based on our current findings suggesting the AR's covariability with surface heat fluxes and CRF, how do these processes in climate models influence the uncertainties in long-term projection by the models?

6. Conclusions

The oceanic precipitating systems of two strong landfalling ARs were studied. AR1 impacted British Columbia, Washington, and Oregon (40°–55°N) during 4–8 January 2009. AR2 influenced Alaska and British Columbia (55°–70°N) during 16–20 January 2009. The ECMWF YOTC data, CMORPH precipitation, and GPCP One-Degree Daily precipitation were used to construct the three-dimensional kinematic and thermodynamic fields. AR1 was between a high pressure center at 32°N, 140°W and a low pressure system extending from 45°N, 158°E to 63°N, 115°W, with an almost west–east orientation. AR2 was between a 850-hPa high pressure region centered at 45°N, 120°W and a 850-hPa low pressure region centered at 52°N, 175°W, with a south–north orientation downstream of a 200-hPa split jet.

Prior to landfall, merging sequential IWV bands over the ocean formed both ARs. This process increased the temperature and moisture content, as well as the actual and saturated vapor pressure of the near-surface air in the ARs. Meanwhile, precipitating convection was amplified. It consumed moisture as well as released latent heat in the path of AR propagation. In both ARs, precipitating convection often revealed vertically tilted Q_1 and Q_2 structures along a horizontal distance around 2000 km. This indicated a spatial transition from a predominant cloud population of shallower convection, to deep convection, to the trailing stratiform deck along the ARs.

However, clear differences existed between the two ARs. First, AR1 traversed a longer distance than AR2 from its tropical moisture reservoir to its midlatitude landfalling location. The precipitating systems in AR1 were mainly distributed on the southwest and northeast sides of the AR. They often revealed significant stratiform types of low-tropospheric level cooling and moistening characteristics of mature convective organizations. Whereas precipitating systems in AR2 continuously covered the main path of the AR, most of the time exhibiting predominantly a deep convection type of heating throughout the troposphere. Second, AR1 had a higher tropopause (around 200 hPa in the AR1 ridge) than AR2 (around 300 hPa in the AR2 ridge). The primary Q_1 extrema in AR1 peaked at higher altitudes with taller heating centers than those in AR2.

In association with these distinctions, the NE Pacific region experienced a heat source and a moisture sink over the AR2 period, but underwent a heat sink and moisture sink despite AR1. It remained, on average, a heat sink and moisture sink in January 2009. This implies that although strong radiative cooling typically dominates the heat budget of the NE Pacific region in January 2009, it could be largely offset by latent heating through strong oceanic precipitation, as seen in AR2. In addition, AR1-IWV had a weaker upward surface latent heat flux and a downward sensible heat flux, as compared to AR2-IWV. The contrast amplified in the AR ridges. This might be related to a relative lack of strong and persistent convection in the excessive warm and moist AR1. Furthermore, dissimilarities in precipitation coverage and the dominant convection types between the two cases also translated to differences in CRF. In AR1-IWV, shortwave cloud forcing C_s and longwave cloud forcing C_l were comparable, resulting in small net CRF. In AR2-IWV, excessive shortwave reflection resulted in a more negative net CRF than AR1.

This study emphasized the roles of oceanic convection embedded in ARs. The case studies showed that the convection not only impacted the moisture transport of ARs, but also modified the heat balance in the midlatitudes through latent heat release, convective heat transport, CRF, and air–sea interactions. Effects of these processes can be used to develop and validate physical parameterizations and simulations of tropical–extratropical interactions in weather and climate models. Therefore, as the next step, statistical significance of the current results must be established and expanded in a climatological study.

Acknowledgments. We thank Robert G. Fovell, Harshvardhan, Frank Lee, and Qianlai Zhuang for stimulating discussions. We appreciate the invaluable comments and corrections by two anonymous reviewers. QL was primarily supported by the China Scholarship Council scholarship; she also acknowledges the Department of Earth, Atmospheric, and Planetary Sciences and the Women in Science Program at Purdue University. Both QL and WT were partially supported by NSF CMMI-1031958 and CMMI-0826119.

REFERENCES

Arakawa, A., and W. H. Schubert, 1974: Interaction of a cumulus cloud ensemble with the large-scale environment, Part I. *J. Atmos. Sci.*, **31**, 674–701, doi:10.1175/1520-0469(1974)031<0674:IOACCE>2.0.CO;2.

Bao, J. W., S. A. Michelson, P. J. Neiman, F. M. Ralph, and J. M. Wilczak, 2006: Interpretation of enhanced integrated water vapor bands associated with extratropical cyclones: Their formation and connection to tropical moisture. *Mon. Wea. Rev.*, **134**, 1063–1080, doi:10.1175/MWR3123.1.

Browning, K. A., 1990: Organization of clouds and precipitation in extratropical cyclones. *Extratropical Cyclones: The Erik Palmén Memorial Volume*, C. Newton and E. Holopainen, Eds., Amer. Meteor. Soc., 129–153.

Carlson, T. N., 1980: Airflow through midlatitude cyclones and the comma cloud pattern. *Mon. Wea. Rev.*, **108**, 1498–1509, doi:10.1175/1520-0493(1980)108<1498:ATMCAT>2.0.CO;2.

Cordeira, J. M., F. M. Ralph, and B. J. Moore, 2013: The development and evolution of two atmospheric rivers in proximity to western North Pacific tropical cyclones in October 2010. *Mon. Wea. Rev.*, **141**, 4234–4255, doi:10.1175/MWR-D-13-00019.1.

Dettinger, M. D., F. M. Ralph, T. Das, P. J. Neiman, and D. R. Cayan, 2011: Atmospheric rivers, floods and the water resources of California. *Water*, **3**, 445–478, doi:10.3390/w3020445.

Ebert, E. E., J. E. Janowiak, and C. Kidd, 2007: Comparison of near-real-time precipitation estimates from satellite observations and numerical models. *Bull. Amer. Meteor. Soc.*, **88**, 47–64, doi:10.1175/BAMS-88-1-47.

Eckhardt, S., A. Stohl, H. Wernli, P. James, C. Forster, and N. Spichtinger, 2004: A 15-year climatology of warm conveyor belts. *J. Climate*, **17**, 218–237, doi:10.1175/1520-0442(2004)017<0218:AYCOWC>2.0.CO;2.

Houze, R. A., Jr., 1989: Observed structure of mesoscale convective systems and implications for large-scale heating. *Quart. J. Roy. Meteor. Soc.*, **115**, 425–461, doi:10.1002/qj.49711548702.

——, 2004: Mesoscale convective systems. *Rev. Geophys.*, **42**, RG4003, doi:10.1029/2004RG000150.

Huffman, G. J., R. F. Adler, M. M. Morrissey, D. T. Bolvin, S. Curtis, R. Joyce, B. McGavock, and J. Susskind, 2001: Global precipitation at one-degree daily resolution from multisatellite observations. *J. Hydrometeor.*, **2**, 36–50, doi:10.1175/1525-7541(2001)002<0036:GPAODD>2.0.CO;2.

Johnson, R. H., 1984: Partitioning tropical heat and moisture budgets into cumulus and mesoscale components: Implications for cumulus parameterization. *Mon. Wea. Rev.*, **112**, 1590–1601, doi:10.1175/1520-0493(1984)112<1590:PTHAMB>2.0.CO;2.

——, P. E. Ciesielski, and T. M. Rickenbach, 2015: A further look at Q1 and Q2 from TOGA COARE. *Multiscale Convection-Coupled Systems in the Tropics: A Tribute to Michio Yanai*, *Meteor. Monogr.*, Amer. Meteor. Soc., in press.

Joos, H., and H. Wernli, 2012: Influence of microphysical processes on the potential vorticity development in a warm conveyor belt: A case-study with the limited-area model COSMO. *Quart. J. Roy. Meteor. Soc.*, **138**, 407–418, doi:10.1002/qj.934.

Joyce, R. J., J. E. Janowiak, P. A. Arkin, and P. Xie, 2004: CMORPH: A method that produces global precipitation estimates from passive microwave and infrared data at high spatial and temporal resolution. *J. Hydrometeor.*, **5**, 487–503, doi:10.1175/1525-7541(2004)005<0487:CAMTPG>2.0.CO;2.

Knippertz, P., and H. Wernli, 2010: A Lagrangian climatology of tropical moisture exports to the Northern Hemispheric extratropics. *J. Climate*, **23**, 987–1003, doi:10.1175/2009JCLI3333.1.

Lavers, D. A., and G. Villarini, 2013: The nexus between atmospheric rivers and extreme precipitation across Europe. *Geophys. Res. Lett.*, **40**, 3259–3264, doi:10.1002/grl.50636.

Luo, H., and M. Yanai, 1984: The large-scale circulation and heat sources over the Tibetan Plateau and surrounding areas during the early summer of 1979. Part II: Heat and moisture budgets. *Mon. Wea. Rev.*, **112**, 966–989, doi:10.1175/1520-0493(1984)112<0966:TLSCAH>2.0.CO;2.

Moncrieff, M. W., 2010: The multiscale organization of moist convection and the intersection of weather and climate. *Climate Dynamics: Why Does Climate Vary? Geophys. Monogr.*, Vol. 189, Amer. Geophys. Union, 3–26, doi:10.1029/2008GM000838.

Neiman, P. J., F. M. Ralph, G. A. Wick, J. D. Lundquist, and M. D. Dettinger, 2008: Meteorological characteristics and overland precipitation impacts of atmospheric rivers affecting the west coast of North America based on eight years of SSM/I satellite observations. *J. Hydrometeor.*, **9**, 22–47, doi:10.1175/2007JHM855.1.

——, L. J. Schick, F. M. Ralph, M. Hughes, and G. A. Wick, 2011: Flooding in western Washington: The connection to atmospheric rivers. *J. Hydrometeor.*, **12**, 1337–1358, doi:10.1175/2011JHM1358.1.

Newell, R. E., N. E. Newell, Y. Zhu, and C. Scott, 1992: Tropospheric rivers?—A pilot study. *Geophys. Res. Lett.*, **19**, 2401–2404, doi:10.1029/92GL02916.

Newman, M., G. N. Kiladis, K. M. Weickmann, F. M. Ralph, and P. D. Sardeshmukh, 2012: Relative contributions of synoptic and low-frequency eddies to time-mean atmospheric moisture transport, including the role of atmospheric rivers. *J. Climate*, **25**, 7341–7361, doi:10.1175/JCLI-D-11-00665.1.

Nitta, T., and S. Esbensen, 1974: Heat and moisture budget analyses using BOMEX data. *Mon. Wea. Rev.*, **102**, 17–28, doi:10.1175/1520-0493(1974)102<0017:HAMBAU>2.0.CO;2.

Pfahl, S., E. Madonna, M. Boettcher, H. Joos, and H. Wernli, 2014: Warm conveyor belts in the ERA-Interim dataset (1979–2010). Part II: Moisture origin and relevance for precipitation. *J. Climate*, **27**, 27–40, doi:10.1175/JCLI-D-13-00223.1.

Ralph, F. M., P. J. Neiman, and G. A. Wick, 2004: Satellite and CALJET aircraft observations of atmospheric rivers over the eastern North Pacific Ocean during the winter of 1997/98. *Mon. Wea. Rev.*, **132**, 1721–1745, doi:10.1175/1520-0493(2004)132<1721:SACAOO>2.0.CO;2.

——, ——, ——, S. I. Gutman, M. D. Dettinger, D. R. Cayan, and A. B. White, 2006: Flooding on California's Russian River: Role of atmospheric rivers. *Geophys. Res. Lett.*, **33**, L13801, doi:10.1029/2006GL026689.

——, ——, G. N. Kiladis, K. Weickmann, and D. W. Reynolds, 2011: A multiscale observational case study of a Pacific atmospheric river exhibiting tropical–extratropical connections and a mesoscale frontal wave. *Mon. Wea. Rev.*, **139**, 1169–1189, doi:10.1175/2010MWR3596.1

Ramanathan, V., R. D. Cess, E. F. Harrison, P. Minnis, B. R. Barkstrom, E. Ahmad, and D. Hartmann, 1989: Cloud-radiative forcing and climate: Results from the Earth Radiation Budget Experiment. *Science*, **243**, 57–63, doi:10.1126/science.243.4887.57.

Ryoo, J. M., D. Waliser, and E. Fetzer, 2011: Trajectory analysis on the origin of air mass and moisture associated with atmospheric rivers over the West Coast of the United States. *Atmos. Chem. Phys. Discuss.*, **11**, 11 109–11 142, doi:10.5194/acpd-11-11109-2011.

Sapiano, M., and P. Arkin, 2009: An intercomparison and validation of high-resolution satellite precipitation estimates with 3-hourly gauge data. *J. Hydrometeor.*, **10**, 149–166, doi:10.1175/2008JHM1052.1.

Schumacher, C., P. E. Ciesielski, and M. H. Zhang, 2008: Tropical cloud heating profiles: Analysis from KWAJEX. *Mon. Wea. Rev.*, **136**, 4289–4300, doi:10.1175/2008MWR2275.1.

Sodemann, H., and A. Stohl, 2013: Moisture origin and meridional transport in atmospheric rivers and their association with multiple cyclones. *Mon. Wea. Rev.*, **141**, 2850–2868, doi:10.1175/MWR-D-12-00256.1.

Tian, Y., C. D. Peters-Lidard, B. J. Choudhury, and M. Garcia, 2007: Multitemporal analysis of TRMM-based satellite precipitation products for land data assimilation applications. *J. Hydrometeor.*, **8**, 1165–1183, doi:10.1175/2007JHM859.1.

Tung, W.-w., C. Lin, B. Chen, M. Yanai, and A. Arakawa, 1999: Basic modes of cumulus heating and drying observed during TOGA-COARE IOP. *Geophys. Res. Lett.*, **26**, 3117–3120, doi:10.1029/1999GL900607.

Waliser, D. E., and M. Moncrieff, 2008: The Year of Tropical Convection (YOTC) Science Plan: A joint WCRP–WWRP/THORPEX international initiative. World Meteorological Organization Rep. WMO/TD-1452, WCRP-130, WWRP/THORPEX-9, 34 pp. [Available online at http://www.ucar.edu/yotc/documents/YOTC˙Science˙Plan.pdf.]

Wu, X., 1994: Diagnostic and semi-prognostic studies of cumulus effects in the presence of mesoscale circulations. *Mon. Wea. Rev.*, **122**, 652–670, doi:10.1175/1520-0493(1994)122<0652:DASSOC>2.0.CO;2.

Yanai, M., and R. H. Johnson, 1993: Impacts of cumulus convection on thermodynamic fields. *The Representation of Cumulus Convection in Numerical Models*, *Meteor. Monogr.*, No. 24, Amer. Meteor. Soc., 39–62.

——, and T. Tomita, 1998: Seasonal and interannual variability of atmospheric heat sources and moisture sinks as determined from NCEP–NCAR reanalysis. *J. Climate*, **11**, 463–482, doi:10.1175/1520-0442(1998)011<0463:SAIVOA>2.0.CO;2.

——, S. Esbensen, and J.-H. Chu, 1973: Determination of bulk properties of tropical cloud clusters from large-scale heat and moisture budgets. *J. Atmos. Sci.*, **30**, 611–627, doi:10.1175/1520-0469(1973)030<0611:DOBPOT>2.0.CO;2.

Zhu, Y., and R. E. Newell, 1994: Atmospheric rivers and bombs. *Geophys. Res. Lett.*, **21**, 1999–2002, doi:10.1029/94GL01710.

——, and ——, 1998: A proposed algorithm for moisture fluxes from atmospheric rivers. *Mon. Wea. Rev.*, **126**, 725–735, doi:10.1175/1520-0493(1998)126<0725:APAFMF>2.0.CO;2.